



Synthetic dispersion interferometry for relative atmospheric pressure sensing

HUGO UITTENBOSCH,^{*} OLIVER KLIEBISCH,^{ID} RAOUL-AMADEUS LORBEER,^{ID} AND PETER MAHNKE

Institute of Technical Physics, German Aerospace Center, Pfaffenwaldring 38-40, 70569 Stuttgart, Germany

**hugo.uittenbosch@dlr.de*

Abstract: We present a modified version of the two-arm, two-color, single second harmonic generation heterodyne dispersion interferometer, as introduced by Irby *et. al.* [Rev. Sci. Instrum. **70**, 699 (1999)]. The amount of optical elements is reduced and digital in-phase and quadrature demodulation is used to retrieve the phase shift from a single photodetector signal. The intrinsic system noise and drift for this device are analyzed by measuring the Allan deviation. We investigate the use of this device for relative atmospheric pressure measurement. Relative pressure measurements are performed in a pressure chamber and referenced against a piezoresistive pressure transceiver to demonstrate the concept. It was found that the deviation was less than 150 Pa and an error estimation has been derived.

Published by Optica Publishing Group under the terms of the [Creative Commons Attribution 4.0 License](#). Further distribution of this work must maintain attribution to the author(s) and the published article's title, journal citation, and DOI.

1. Introduction

In aviation, the barometric or density height is used as a reference figure for the altitude of an aircraft, rather than the height above ground level, since the change of pressure over height within the troposphere is well-behaved and modeled by the International Standard Atmosphere (ISA) equations [1].

Modern aircraft determine the ambient pressure via static pressure ports located on the fuselage or via Pitot tubes mounted at the front of the aircraft [2]. However, while these systems have been tested and used in practice for decades, they are prone to failure in icing conditions without sufficient heating and will continue to report pressure measurements, albeit being incorrect [3]. Therefore, a method is of interest which can determine the static pressure optically and is resilient against mechanical and environmental perturbations, while also featuring self-diagnosis in regards to measurement degradation and errors. There are optical techniques that allow the contact-less measurement of the static ambient pressure. These include spectroscopic techniques like tunable diode laser absorption spectroscopy (TDLAS) [4,5] and filtered Rayleigh spectroscopy (FRS) [6]. In theory, the failure of such a system, e.g., in the case of icing, can be more easily discerned due to a drop in signal strength or the total loss of signal.

Another approach to measure the static ambient pressure is via the pressure-dependent refractivity of air. This connection has been extensively researched by Edlen in 1966, Owens in 1967 and Ciddor in 1996 [7–9]. The semi-empirical relations published by Ciddor allow the calculation of the refractive index of air depending on the wavelength λ , the ambient pressure p and temperature T , as well as the relative humidity rh and the carbon dioxide (CO_2) content η_c , that is $n = n(\lambda, p, T, rh, \eta_c)$, for a wide range of conditions. Vice-versa, given a change in the refractive index, a change of the atmospheric parameters can be calculated.

The optical dispersion interferometer (DI) uses a single-arm, two-color, homodyne interferometer to detect changes in the dispersive properties of a medium between two second harmonic generation (SHG) crystals. The main advantage of this interferometer is the collinear single-arm

design which enables a high resistance against mechanical vibrations [10,11]. An overview of different implementations of the traditional DI using homodyne or heterodyne detection is given by Akiyama et al. (2020) [12]. The concept of using such a device for the measurement of the dispersion of air has been investigated by, e.g., Drachev (1990) and Brandi et al. (2007) [13,14].

A two-arm, two-color, heterodyne interferometer with single SHG for dispersion measurement has been proposed by Irby et al. (1999) and more recently by Lee et al. (2021) [15,16]. The second optical frequency doubling via a nonlinear crystal is replaced by an electrical frequency doubler in both cases. This type of setup avoids the technical challenge of aligning the probe beam onto the aperture of the second nonlinear crystal [16]. Due to the strong similarity to the single-arm DI we refer to this type of device as synthetic dispersion interferometer (SDI).

In this work, a SDI setup is presented, which utilizes the integer factor in the Bragg equation to generate a reference beam from an acousto-optic modulator (AOM) with a single driver frequency that contains both the modulated fundamental and second harmonic (SH) beam. This allows for a compact heterodyne interferometer where the radio frequency (RF) beat signals for the fundamental and SH beam are detected with a single detector one octave apart from each other. In addition, a beam splitter is placed such that the reflected probe beam is aligned back into itself and onto the reference beam, further reducing the amount of required optical elements. By two-tone downmixing the photo detector (PD) signal is down-shifted to a lower signal bandwidth for easier analog-to-digital conversion and followed by digital in-phase and quadrature (IQ) demodulation to recover the pressure-dependent phase difference.

The system noise and stability of this device are examined by evaluating the Allan deviation, as well as the power spectral density (PSD). The setup is then used to measure the static pressure in an airtight chamber, which is vented at different rates, and compared against a piezoresistive pressure sensor. The deviation between both systems is shown to be below 1.5 hPa.

2. Materials and methods

2.1. Experimental setup

2.1.1. Optical setup

A continuous wave (cw) diode-pumped solid-state (DPSS) Nd:YAG single longitudinal mode (SLM) laser with intracavity frequency doubling (CNI Laser MSL-FN-532-10mW) is used for this system. The wavelengths and output powers are summarized in Table 1. Both the fundamental laser frequency and the SH beam operate in the TEM₀₀ transversal mode. The coherence length for both wavelengths is approximately 50 m in comparison to the path length difference of the SDI, which is less than 2.5 m. A schematic of the experimental setup is displayed in Fig. 1. The main reason for choosing the specified wavelengths is the applicability of the Ciddor equation, which holds for $\lambda \in [300, 1690]$ nm [9], and the availability of components optimized for this wavelength range.

Table 1. Laser parameters

Parameter	Value	
Fundamental	Wavelength	1064 nm
	Power	36.22 mW
Second harmonic	Wavelength	532 nm
	Power	10.64 mW

The laser source is not compensated for walk-off between the fundamental and SH beam. Therefore, a small angle between both beams exists. Whilst being small in practice ($\alpha \approx 0.05^\circ$), this deviation can introduce non-common path errors into the system. A wedged prism pair (WPP) is aligned at the exit of the laser module such that the prism dispersion realigns the beams.

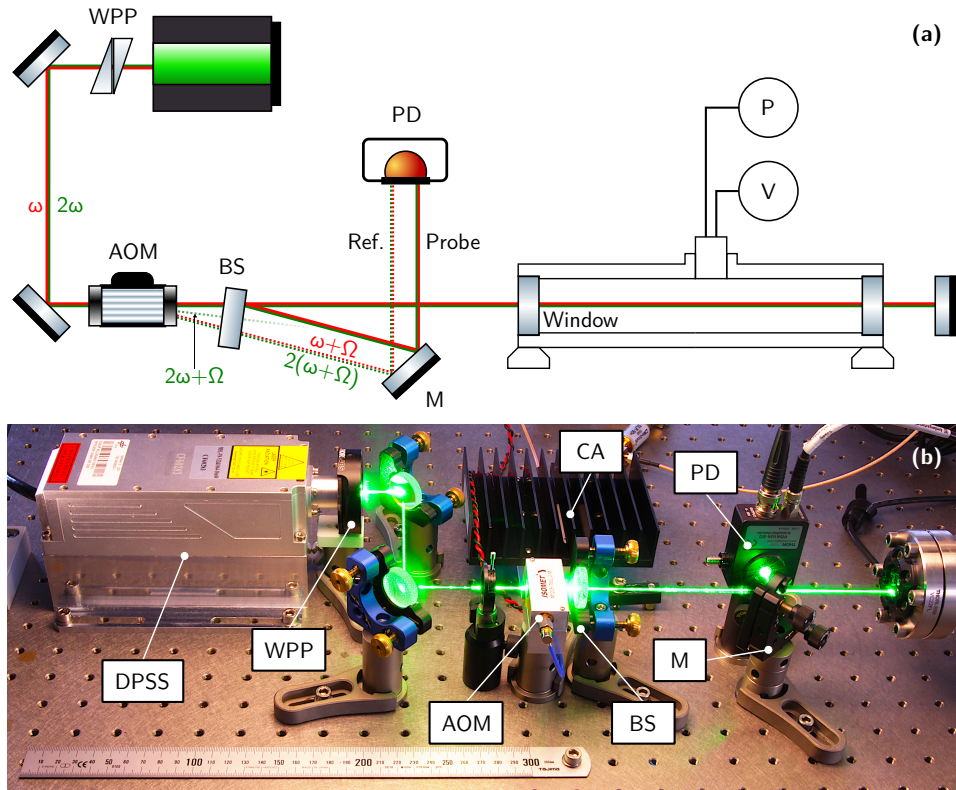


Fig. 1. (a) Schematic of the optical setup. The fundamental (red) and SH (green) beam are realigned using a WPP and aligned through the AOM via two kinematic mirrors. The unmodulated portion of the fundamental and second harmonic is used as the probe beam, whereas the modulated first and second order diffractions generated by the AOM are picked off by a mirror and used as the reference beam (dotted). The probe beam enters the pressure chamber and is reflected back into itself, passing the chamber twice. When the probe beam hits the BS from the opposite side, a part of it is reflected and diverted onto the PD via a D-shaped mirror (M), together with the reference beam. The chamber pressure is monitored separately by a pressure (P) sensor and can be raised after evacuation by opening the control valve (V). The geometric proportions of the optical paths in this schematic are exaggerated for the purpose of illustration. (b) Image of the laboratory setup. Not shown are the full pressure chamber and the return mirror. The coaxial amplifier (CA) is placed close to the AOM to minimize electromagnetic interference. The iris in front of the AOM is used during initial alignment only.

Since this correction is applied immediately after the laser, both beams are coaxial for the relevant interferometer arm length.

Two mirrors are used to adjust the beam path through the AOM (ISOMET M1205-T80L), which is operated at 80 MHz and anti-reflex (AR) coated for both wavelengths. The adjustment of the diffraction order efficiency is performed qualitatively via the alignment of the beam through the AOM using the kinematic mirror mounts. For $\sin \theta_m \approx \theta_m$ and under Bragg angle θ_B , the angles under which an incident beam is diffracted by an AOM are

$$\theta_m \cong \frac{m \cdot \lambda}{n \cdot \Lambda} = 2 \cdot m \cdot \theta_B, \quad (1)$$

where $m \in \mathbb{Z}$ are the diffraction orders, n is the refractive index of the crystal and Λ is the acoustic wavelength within the crystal [17]. Further, the frequency shift of the diffracted light is

$$\Omega_{\text{AOM}} = m \cdot \Omega_{\text{mod}}, \quad (2)$$

where Ω_{mod} is the acoustic modulation frequency [17]. Thus, if all material parameters are considered equal and $\lambda_{\omega} = 2 \cdot \lambda_{2\omega}$, then

$$\theta_{m=1}(\lambda_{\omega}) = \theta_{m=2}(\lambda_{2\omega}), \quad (3)$$

that is the first diffraction order of the fundamental laser frequency is diffracted at the same angle as the second diffraction order of the SH beam. Consequently, the reference beam can be generated from this common diffraction angle and the modulation of the diffracted SH beam is twice that of the fundamental. Hereby, the dual frequency AOM driver signal used by Irby et al. can be avoided [15].

The optical paths after the AOM are displayed schematically in Fig. 1(a). A 50:50 plate beam splitter (BS) (Thorlabs BSW26) is placed in close proximity behind the AOM. The coated BS side faces away from the AOM and towards the return mirror at the end of the probe beam path. The fundamental and SH, as well as the modulated reference beam, pass through the BS. The measured beam separation angle between the probe and reference after the BS is $\theta \approx 1.2^\circ$. The optical powers in the probe and reference beam are $P_{\omega} \approx 11.5$ mW and $P_{2\omega} \approx 2.3$ mW and $P_{\omega+\Omega} \approx 3.7$ mW and $P_{2(\omega+\Omega)} \approx 0.45$ mW, respectively.

The probe beam travels through the pressure chamber and is reflected back into itself using a plane mirror. A part of the probe beam is then reflected by the BS, which is placed at such an angle that the reflected probe beam and the reference beam are aligned parallel and with minimal offset. A D-shaped mirror (M) is used to pick off the reference and probe beam and align them onto the PD (Thorlabs PDA10A-EC). Since the return beam can propagate back into the laser resonator if the setup is adjusted ideally, a slight misalignment is tolerated, such that the return beam misses the laser exit aperture while still having sufficient signal-to-noise ratio (SNR) for demodulation. The footprint of the interferometer, excluding the pressure chamber and return mirror, is less than 500 mm by 300 mm as can be seen in Fig. 1(b). Single-arm DIs with two SHG crystals can reach a similar form factor [18,19].

2.1.2. Electrical setup

The AOM driver is a Rigol DSG815 signal generator (SG) which generates an 80 MHz sine wave with -20 dBm up to -5 dBm. This signal is amplified by 33 dB in a CA (Mini-Circuits ZHL-1-2W). As per Eq. (2), the maximum frequency shift is 160 MHz for the second diffraction order of the SH beam. The PD has a 3 dB bandwidth of 150 MHz and can hence capture the RF beat signal. However, this much bandwidth is not needed in the context of this work. In order to reduce the analog-to-digital converter (ADC) sample rate requirements, the DI signal is downmixed below 1 MHz using a dual comb signal generated by two channels of a Tektronix AFG3252 SG, which is referenced to a 10 MHz phase-locked loop (PLL) clock signal. The clock signal is provided by the AOM driver and is amplified and shared by a SRS FS730 distribution amplifier (DA). The downmixing SG generates two sinusoidal signals with

$$f_1 = f_0 - \Delta f_1 = 79.875 \text{ MHz}, \quad (4)$$

$$f_2 = 2 \cdot (f_0 - \Delta f_1) = 159.75 \text{ MHz}, \quad (5)$$

where $f_0 = 80$ MHz and $\Delta f_1 = 125$ kHz. These are combined in a power splitter and then mixed with the DI signal. This causes the signal to be downmixed to the new kHz carrier frequencies, that is Δf_1 and $2\Delta f_1$. Higher harmonics resulting from the mixing are suppressed using a low-pass

filter (LPF). All phase relations are maintained during this procedure. The signal is then sampled by an 1 MSps ADC with a bit depth of 12 bit, which is also referenced to one of the 10 MHz DA PLL clocks.

2.1.3. Pressure chamber and reference sensor

The pressure chamber has an internal diameter of 40 mm and a length of 1083 mm. The windows that allow the probe beam to pass through the chamber are AR coated for 532 nm and 1064 nm and not wedged. A manual needle valve (Pfeiffer EVN116) can be used to control the inflow of air into the chamber. The latter is connected to a vacuum pump via a secondary valve, which is closed off after the chamber has been evacuated to within a few Pa. The reference device is a piezoresistive pressure transceiver (Keller Series 33X) with a full-scale of 10^5 Pa and ± 50 Pa accuracy. The total calibrated error is specified to be ≤ 50 Pa for temperatures between 10°C and 40°C . The sensor bandwidth is not specified. The transducer is mounted in vicinity to the needle valve and also features an integrated temperature sensor with a resolution of $\leq 0.01^\circ\text{C}$ and an accuracy of $\leq \pm 2^\circ\text{C}$.

2.2. Methods

2.2.1. Refractivity of air

The accumulated phase for the reference and probe beam at the detector must be modeled for λ_ω and $\lambda_{2\omega}$ separately, since the modulation frequency is different for each. The phase modulated onto the carrier frequency Ω_{AOM} between the reference and probe beam for λ_ω is

$$\hat{\varphi}_\omega(t) = \underbrace{(\omega + \Omega) \cdot t}_{\text{Ref.}} - \underbrace{\left(\omega t - \frac{2\pi}{\lambda_\omega} \int_{h=0}^l n(\lambda_\omega) dh \right)}_{\text{Probe}} + \Phi_{\text{NCP},\omega}, \quad (6)$$

where Φ_{NCP} denotes the “non-common path” phase difference. Similarly for $\lambda_{2\omega}$,

$$\hat{\varphi}_{2\omega}(t) = 2(\omega + \Omega) \cdot t - \left(2\omega t - \frac{2\pi}{\lambda_{2\omega}} \int_{h=0}^l n(\lambda_{2\omega}) dh \right) + \Phi_{\text{NCP},2\omega}. \quad (7)$$

For simplicity it is assumed that the “non-common path” phase contributions are constant and can be calibrated to zero. With $\Delta\varphi = \hat{\varphi}_{2\omega} - 2 \cdot \hat{\varphi}_\omega$ and $\lambda_\omega = 2 \cdot \lambda_{2\omega}$ it follows that

$$\Delta\varphi = \frac{2\pi}{\lambda_{2\omega}} \cdot \int_{h=0}^l [n(\lambda_{2\omega}, p, T, rh, \eta_c, h) - n(\lambda_\omega, p, T, rh, \eta_c, h)] dh, \quad (8)$$

where the refractive index varies along the length of the probe path h with a total (two-way) length of l . In practice it is assumed that n is constant along h . The same is also postulated for the CO_2 content η_c , for which 450 ppm is assumed in accordance to the Ciddor equation [9]. Considering this, Eq. (8) simplifies to

$$\Delta\varphi - \frac{2\pi \cdot l}{\lambda_{2\omega}} \cdot [n(\lambda_{2\omega}, p, T, rh) - n(\lambda_\omega, p, T, rh)] = 0. \quad (9)$$

For a given $\Delta\varphi$ this equation can be solved numerically for p , if the ambient temperature and humidity are known.

2.2.2. IQ demodulation

In practice, the phase difference can not be extracted from the measured signal directly since the phase information is contained in a single two-tone signal at different carrier frequencies. Note

that due to the downmixing described in Sec. 2.1.2, the carrier frequencies are now $\Omega = \Delta f_1$ and $2\Omega = 2\Delta f_1$. The PD signal can be modeled as

$$I_{\text{photo}}(t) = R(\lambda_{2\omega}) \cdot [P_{2\omega,R} + P_{2\omega,P} + 2 \underbrace{\sqrt{P_{2\omega,R} \cdot P_{2\omega,M}}}_{A_{2\omega}} \cdot \cos(\hat{\varphi}_{2\omega})] + R(\lambda_{\omega}) \cdot [P_{\omega,R} + P_{\omega,P} + 2 \underbrace{\sqrt{P_{\omega,R} \cdot P_{\omega,M}}}_{A_{\omega}} \cdot \cos(\hat{\varphi}_{\omega})], \quad (10)$$

where $R(\lambda)$ is the PD responsivity in [A/W] and P is the optical power. The indices R and P denote the reference and probe beam, respectively. To obtain the phase, i.e., $\varphi_{\omega} = \hat{\varphi}_{\omega} - \Omega t$, the signal $I_{\text{photo}}(t)$ must be IQ demodulated. This step is applied digitally after the signal has been sampled by the ADC and is displayed schematically in Fig. 2. The two-tone signal is mixed with the sine and cosine of Ω and 2Ω , respectively, and filtered using LPFs. The results are the I and Q components of $\hat{\varphi}_{\omega}$ and $\hat{\varphi}_{2\omega}$, which are used to determine φ_{ω} and $\varphi_{2\omega}$. Exemplary, the IQ-mixer to determine φ_{ω} is represented by means of complex multiplication as

$$\begin{aligned} I + j \cdot Q &= \text{LPF}[\{\cos(\Omega t) + j \sin(\Omega t)\} \cdot 2A_{\omega} \cdot \cos(\hat{\varphi}_{\omega}(t))] \\ &= \text{LPF}[e^{j\Omega t} \cdot 2A_{\omega} \cdot \cos(\hat{\varphi}_{\omega}(t))] \\ &= \text{LPF}[e^{j\Omega t} \cdot (e^{j\hat{\varphi}_{\omega}(t)} + e^{-j\hat{\varphi}_{\omega}(t)}) \cdot A_{\omega}] \\ &= A_{\omega} \cdot e^{j(\Omega t - \hat{\varphi}_{\omega}(t))} = A_{\omega} \cdot e^{-j\varphi_{\omega}(t)} \\ &= A_{\omega} \cdot [\cos(\varphi_{\omega}(t)) - j \sin(\varphi_{\omega}(t))]. \end{aligned} \quad (11)$$

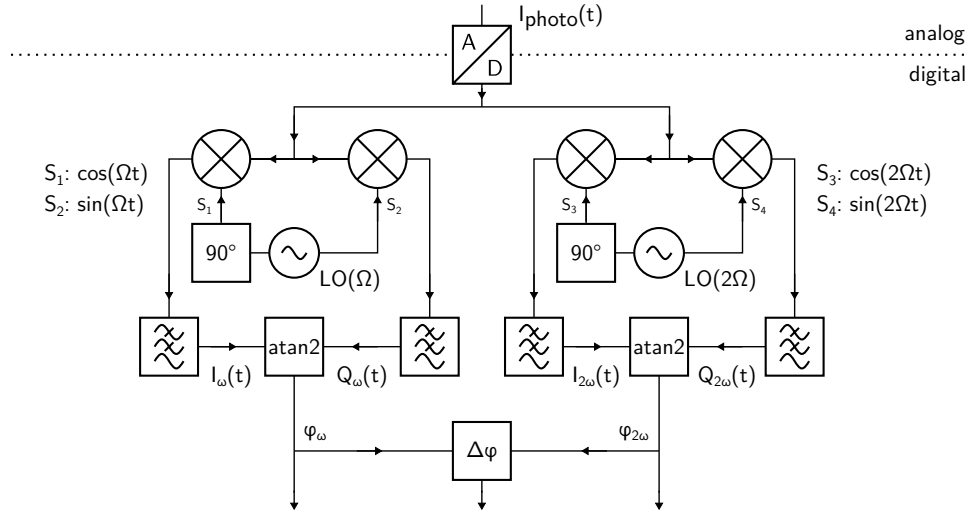


Fig. 2. Digital IQ demodulation schematic: the digitized PD signal is mixed with sine and cosine local oscillators (LOs) with $\Omega = \Delta f_1$ and 2Ω , respectively. This results in the I and Q components for the fundamental and SH laser beams. After passing through digital LPFs, the phase shifts are calculated as $\varphi = \arctan2(I, Q)$. The total phase shift is $\Delta\varphi = \varphi_{2\omega} - 2 \cdot \varphi_{\omega}$, which is analogous to the second optical frequency doubling process in a classic DI.

A_{ω} is the magnitude of the IQ signal. The operator $\text{LPF}[\dots]$ represents an ideal filter that removes all frequencies larger than $\Omega t - \hat{\varphi}(t)$. The phase can be calculated using the 2-argument

arctangent for both φ_ω and $\varphi_{2\omega}$ via

$$\varphi = \arctan2(I, Q) = \underbrace{\Im\{\ln(I + jQ)\}}_{=z}. \quad (12)$$

The second definition of the phase as the imaginary part of the natural logarithm of I and Q will be useful further on. The main benefit of performing the IQ demodulation digitally is the ability to not only output $\Delta\varphi$, but also the individual phases for the fundamental and SH beam, as well as the length of the respective phasors, that is $|z|$.

For this work, the demodulation is performed off-line after ADC acquisition on a separate computer. Five minutes of measured data, i.e., $3 \cdot 10^8$ data points, can be demodulated within two minutes on a i7-10610U CPU. The demodulation scheme described above is implemented in the Julia programming language [20].

2.2.3. Phase deviation analysis

In order to characterize the behavior of the interferometer for extended time periods, minutes in the case of this work, a suitable metric is needed. Commonly, for systems that are assumed to be dominated by white noise, the standard variance $\mu = \sigma^2$ is used. However, this quantity can diverge if the signal source drifts over time, or is prone to some form of bias [21, p. 13]. For this reason, the Allan deviation $\sigma_y(\tau)$ is utilized. Originally developed to evaluate the frequency stability of atomic clocks, this metric can be interpreted as the local deviation from the mean depending on the width of an averaging window τ [22]. This method has been modified from its original field of oscillator analysis and is now used to determine the stability of various sensors, i.e., inertial measurement units (IMUs) [23]. Adapted from this, the analogous, modified, overlapping Allan variance for the DI phase measurements is defined as

$$\sigma_{\Delta\varphi}^2(\tau) = \frac{1}{2m^4 \cdot (M - 3m + 2)} \cdot \sum_{j=1}^{M-3m+2} \left(\sum_{i=j}^{j+m-1} \left[\sum_{k=i}^{i+m-1} \Delta\varphi_{k+m} - \Delta\varphi_k \right] \right)^2, \quad (13)$$

where $\Delta\varphi_i$ with $i = 1, \dots, M$ are the phase measurements and $\tau = m \cdot \tau_0$ is the averaging time, with τ_0 being the measurement time interval. This version of the Allan deviation was chosen since it can better discern between flicker and white noise [21, p. 17]. Additionally, the PSD for the phase signal is calculated via

$$S\left(\frac{k}{M \cdot \tau_0}\right) = \frac{2\tau_0}{M} \cdot \left| \sum_{g=1}^M \Delta\varphi_i \cdot \exp\left[-2\pi j \cdot \frac{gk}{M}\right] \right|^2, \quad (14)$$

where $f = k/(M \cdot \tau_0)$ and $k = 0, \dots, M/2$. This method will also be used to analyze the system noise.

3. Results

3.1. Phase deviation

In order to characterize the intrinsic system noise and drift prior to the pressure measurements, the phase difference is measured under static conditions. Several measures were taken to minimize external influences as much as possible. To minimize the effect of external dispersive influences, the chamber is evacuated to a residual pressure of approx. 10^3 Pa before static measurements are performed. The laser and AOM are operated for 2 hours in advance to achieve a stable thermal state. In addition, the setup is mounted on an optical table with vibration dampening. The chamber pressure is monitored using the piezoresistive pressure sensor and for the duration of

the static measurements the internal pressure did not change more than 5 Pa. Data was collected over a duration of 5 min for increasing AOM driver power. Using Eq. (13), the Allan deviation can be calculated and is displayed in Fig. 3. The AOM driver power denoted includes the 33 dB CA amplification.

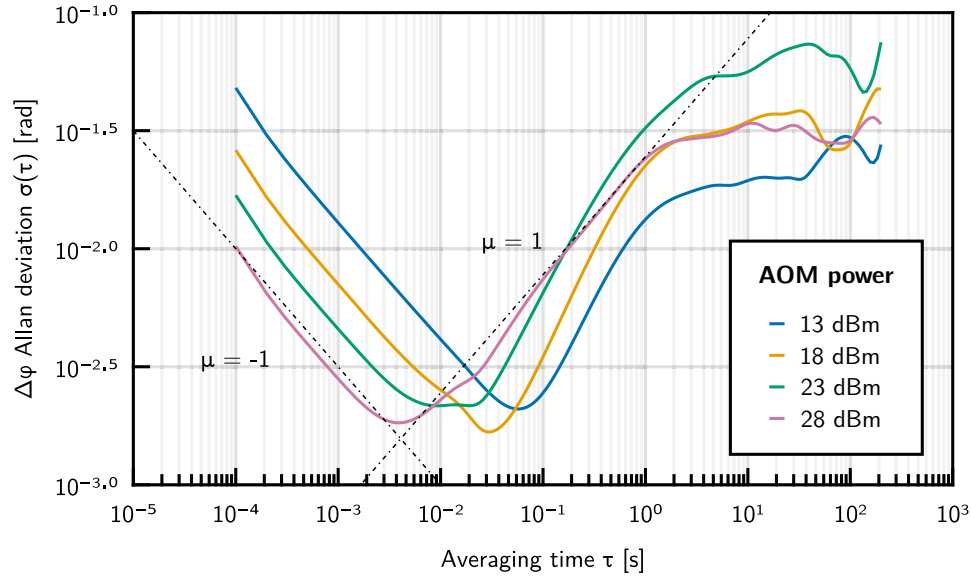


Fig. 3. Allan deviation of the DI difference phase $\Delta\varphi$ measured over a duration of 5 min at different AOM driver power settings. Guide lines for white noise ($\mu = -1$) and random walk noise ($\mu = 1$) have been added.

It can be observed that an increase in AOM driver power has three effects: the noise floor on the left flank is lowered and the deviation minimum tends towards shorter averaging times. Conversely, the influence of drift-like effects on the right flank increases as well. In the averaging time domain, noise sources can be modeled as

$$\sigma(\tau) \propto \tau^{\frac{\mu}{2}}, \quad (15)$$

where $\mu = -1$ corresponds to white noise and $\mu = 1$ to random walk noise [21, p. 9]. Guide lines with these values have been added to Fig. 3 for the 28 dBm curve. Since the SNR at this AOM driver power setting was highest, it is used for the pressure measurements. The minimal deviation for this operating point is on the order of 1 mrad for $\tau \approx 4$ ms. However, the presence of random walk noise, which levels off at around 1 s of averaging, increases the minimal achievable deviation.

The timeseries data for $\Delta\varphi$ is shown in detail for the aforementioned AOM driver power in Fig. 4(a) and the phasor length $|z|$ for φ_ω and $\varphi_{2\omega}$ is displayed in Fig. 4(b) and Fig. 4(c), respectively. Notably, $|z_\omega|$ is much greater than $|z_{2\omega}|$. Some temporally correlating events can be seen, i.e., a sharp drop in $|z_\omega|$ at $t \approx 145$ s correlating with a significant change in phase, marked by a dotted black line.

The PSD of $\Delta\varphi$, as defined in Eq. (14), is presented in Fig. 4(d). In the frequency domain, noise sources can be modeled via

$$S(f) \propto f^\alpha. \quad (16)$$

A direct relation between the noise models for τ and f in the form of $\mu = -\alpha - 1$ exists [21, p. 10]. Thus, guide lines have also been added to the PSD for $\alpha = 0$ and $\alpha = -2$. A peak in

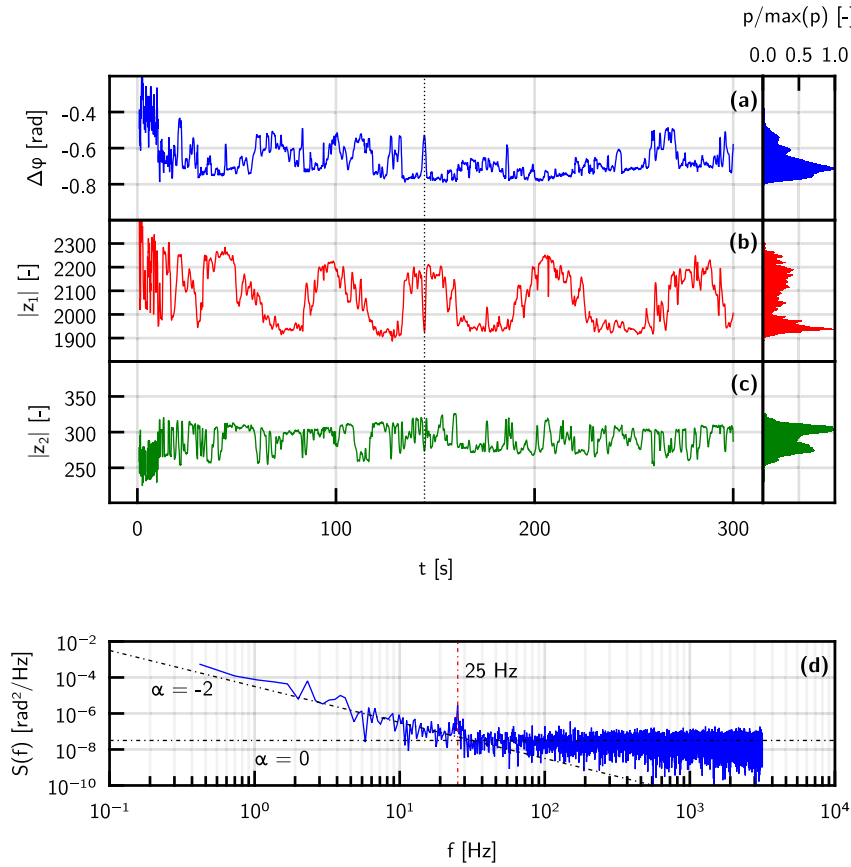


Fig. 4. Phase noise measurement for 28 dBm AOM driver power. The data for $\Delta\varphi$ is displayed in (a), along with the length of the phasors for φ_{ω} and $\varphi_{2\omega}$ in (b) and (c), respectively. The normalized probability density functions (PDFs) are shown to the right. A strong deviation of the distributions from an ideal white noise source can be seen. The PSD of $\Delta\varphi$ is depicted in (d). Guide lines with $\alpha = -2$ (random walk noise) and $\alpha = 0$ (white noise) have been added. The peak at 25 Hz is caused by an external acoustic disturbance.

the PSD can be observed at 25 Hz in the transition region. The source for this perturbation was found to be an external acoustic excitation and was detected with a microphone as well. Despite our best efforts, a coupling of this disturbance into the experimental setup could not be avoided. However, this does not pose a problem for the pressure measurements presented below since the disturbance is outside the bandwidth of interest and can be filtered out.

3.2. Pressure measurements

In order to conduct the pressure measurements the chamber is evacuated to a residual pressure below 10^2 Pa and sealed off. The piezoresistive pressure sensor is used to measure the internal pressure and temperature. The relative humidity of the ambient air is maintained at 50% by an air conditioning system and monitored via a humidity sensor. The valve inflow rate is set such that the pressure change rate remains within the bandwidth of the piezoresistive transceiver and the linear inflow regime of the valve. Pressure rates between 60 Pa/s and 600 Pa/s were considered, which corresponds to an aircraft descent rate of 14.7 m/s and 147 m/s at a height of 10 km. The measurement is initiated in this static state, such that the starting pressure of the DI can be

referenced to that of the absolute sensor. The valve is then opened and data is recorded until a total length of 5 min is reached. The resulting phase data is used to calculate the pressure change according to Eq. (9). The equation is solved numerically for the pressure p using a Nelder-Mead optimizer [24]. Since the temperature profile recorded during the measurements never varied more than 0.25°C , the average value \bar{T} over the measurement duration is used to calculate the refractive index via the Ciddor equation. For the relative humidity the value of 50% mentioned above is used and the pressure chamber length $l = 1083$ mm is assumed as the one-way probe path length. The results are shown in Fig. 5(a), with the reference sensor curves being displayed as colored dashed lines. The calculated values for the DI are overlaid as black lines. The starting pressure value for the interferometer at $t = 0$ s is matched to the initial absolute measurement of the reference sensor.

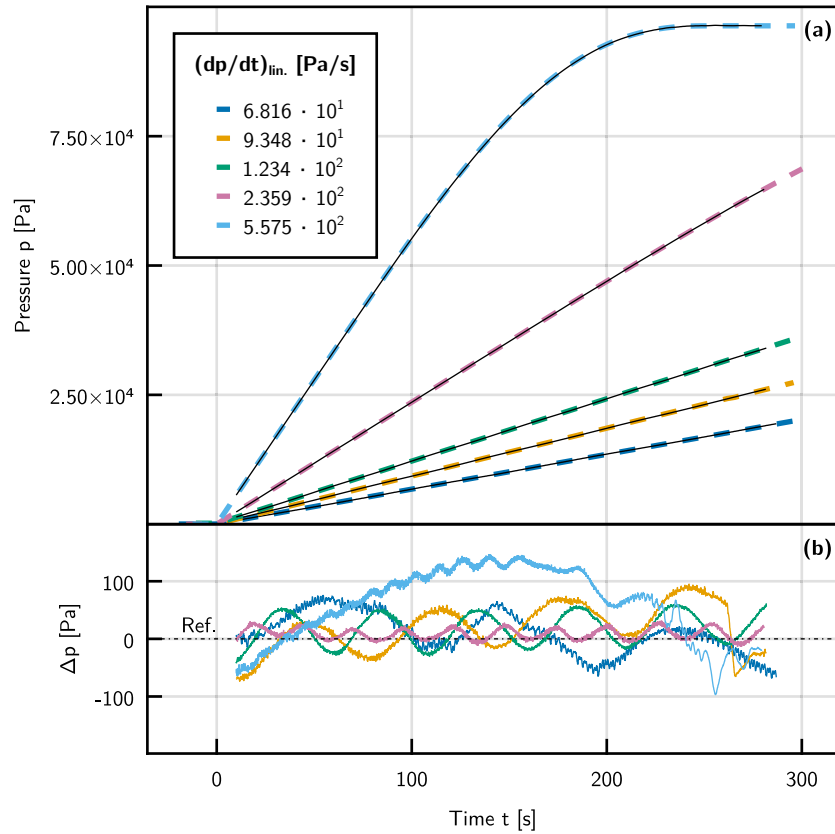


Fig. 5. Pressure measurements at different valve settings. The reference sensor pressure data is displayed in (a) as colored dashed lines. The calculated DI pressure data is referenced to the absolute pressure of the piezoresistive sensor at $t = 0$ and plotted as black lines. The DI data rate has been adjusted to that of the reference sensor (10 Hz). The pressure change rate $(dp/dt)_{lin.}$ is given for the linear range of each measurement. The difference Δp between the reference sensor and the DI is shown in (b) for better comparability. The line color refers to (a).

Since the data output sample rate of the reference sensor is 10 Hz, the DI pressure data is downsampled and averaged from a rate of 10 kHz after demodulation to a bandwidth of 10 Hz for the sake of comparability. The difference $\Delta p = p_{Ref.} - p_{DI}$ between the pressure calculated from the DI and that measured by the transceiver is displayed in Fig. 5(b). It can be seen that the

discrepancy between both systems is less than 100 Pa for all measurements, except for an inflow rate of 557.5 Pa/s. Here, the inflow rate behaves nonlinearly as the pressure difference between the chamber and the environment decreases and Δp reaches up to 140 Pa.

4. Discussion

The experimental investigation of the noise behavior has shown that the system exhibits random walk drift, as can be seen in Fig. 3 or Fig. 4(d). For instance, the sudden changes in the measured $\Delta\varphi$ of up to 200 mrad that can be seen in Fig. 4(a) would correspond to a pressure change of 194 Pa, a behavior which can not be explained by realistic changes in pressure under the experimental conditions described in Sec. 3.1.

However, this has not been found to lead to major deviations from the reference probe pressure reading when conducting venting experiments with changing pressure, as can be seen in Fig. 5(b). While there is some form of oscillation modulated onto the pressure differences, it remains smaller in value and is of periodic nature, as opposed to the issue described above. Therefore, the effect of errors on the IQ-phasor in relation to its magnitude is discussed below.

4.1. Phase error estimation

Based on Eq. (12), the error $\delta\phi$ of the demodulated phase is dependent on the error of the phase vector δz and thus

$$\delta\varphi = \Im \left(\frac{d}{dz} \ln(z) \cdot \delta z \right) = \Im \left(\frac{\delta z}{z} \right) \quad (17)$$

$$= \frac{1}{2j} \cdot \left(\frac{\delta z}{z} - \frac{\delta z^*}{z^*} \right) \quad (18)$$

$$= \frac{1}{2j} \left(\frac{(\delta I + j\delta Q)(I - jQ) - (\delta I - j\delta Q)(I + jQ)}{I^2 + Q^2} \right) \quad (19)$$

$$= \frac{Q \cdot \delta I + I \cdot \delta Q}{I^2 + Q^2}. \quad (20)$$

In general, the uncertainty of each phase scales with $\frac{|\delta z|}{|z|}$ as per Eq. (17) and, therefore, the length of the respective phasor, which is $|z|$, can be used as a measure of uncertainty for φ_ω and $\varphi_{2\omega}$, with the uncertainty of the difference phase being

$$\delta\Delta\varphi = |\delta\varphi_{2\omega}| + 2 \cdot |\delta\varphi_\omega|. \quad (21)$$

In terms of the phase difference shown in Fig. 4(a), this means the following: for the individual phases, the uncertainty is determined on the basis of the $|z_1|$ and $|z_2|$, whereby the definition of the respective $|\delta z|$ must be done manually due to the distributions shown in Fig. 4(b) and Fig. 4(c).

For $\delta\varphi_\omega$, the length of the phasor is derived from the peak of the distribution ($|z_1| \approx 1938$), and the magnitude of δz_1 is derived from the $\min(|z_1|) \approx 1900$ and $\max(|z_1|) \approx 2300$. The resulting uncertainty is

$$\delta\varphi_\omega = \frac{|\delta z_1|}{|z_1|} = \frac{\max(|z_1|) - \min(|z_1|)}{|z_1|} \approx 206.4 \text{ mrad}. \quad (22)$$

The same procedure is applied to $\delta\varphi_{2\omega}$, where $|z_2|$ is read from the global maximum of the distribution shown in Fig. 4(c). It follows that $\delta\varphi_{2\omega} \approx 313.5$ mrad and hence $\delta\varphi \approx 833.4$ mrad. However, it must be noted that this result reflects the worst-case uncertainty since almost all outliers are included into this calculation. Depending on the time frame, $\delta\varphi$ is significantly lower on a local scale or after averaging. The results for the experimental characterization of the uncertainty in Fig. 3 show that for an AOM driver power of 28 dBm an uncertainty of less

than 3 mrad ($\cong 3$ Pa) can be achieved on the millisecond timescale. Beyond this, however, the influence of drift and outlier effects increases, raising the uncertainty to about 30 mrad ($\cong 30$ Pa) before converging. The order of this value agrees in good approximation with the deviation of the pressure change experiment. Nevertheless, the magnitude of the phasors can be used as a tool for self-diagnosis, enabling pressure measurements with a physically based figure of merit in future experiments.

It can be argued that the fluctuations in the difference phase are partly explained by fluctuations in the magnitude of the phasors. The intermittent correlation of the disturbances in the amplitudes suggests that they are caused by disturbances in the laser source. The targeted misalignment of the setup, as described in Sec. 2.1.1, might not be fully sufficient to avoid interfering with the laser in operation.

4.2. Theoretical sensitivity

As to the theoretical limitations of a DI for relative pressure measurement, the achievable accuracy as a function of the probe path length and under standard conditions can be estimated as

$$\frac{\Delta\varphi}{p_0 \cdot l} = \frac{2\pi}{\lambda_{2\omega}} \cdot \frac{n(\lambda_{2\omega}, p_0, T_0, rh) - n(\lambda_{\omega}, p_0, T_0, rh)}{p_0}, \quad (23)$$

based on Eq. (9). For the laser parameters presented above and $p_0 = 101325$ Pa, $T_0 = 15^\circ\text{C}$, $rh = 0.5$ a sensitivity of $4.934 \cdot 10^{-4}$ rad m⁻¹ Pa⁻¹ is calculated. This means that for a pressure sensitivity of 1 Pa and $l = 2$ m, a phase sensitivity of roughly 1 mrad is necessary. Therefore, by scaling the probe path length, the sensitivity can be adjusted to fit variable requirements, but at the cost of higher susceptibility to non-common path phase errors.

Regarding the phase shift caused by dispersive elements following the AOM, e.g., the BS, it can be said that the influence should be constant and deductible as long as the dispersion does not change during the measurement, i.e., due to temperature variations. In addition, it is assumed that the CO₂ content η_c is approximately 450 ppm. This value can vary over height and time within the atmosphere and for a change of ± 100 ppm around the assumed value the change in refractive index is approximately $\pm 1.5 \cdot 10^{-8}$ as per the Ciddor equation. This corresponds to a change in pressure of approximately ± 6 Pa. Hence, the CO₂ concentration needs to be considered to reach single-digit Pa accuracy for the theoretical sensitivity calculated above.

Further, to simplify Eq. (9), it is also assumed that $n = \text{const.}$ along of the probe beam path. This places constraints on the positioning of the probe path, whereby strong local pressure gradients should be avoided to measure the static pressure. With respect to our experimental setup, a deformation of the cell or the rubber window gaskets due to the differential pressure needs to be considered. As per Eq. (9) the difference phase scales linearly with the probe path length l and hence the relative error with respect to l is

$$\frac{\delta\Delta\varphi}{\Delta\varphi} = \frac{1}{\Delta\varphi} \cdot \frac{\partial\Delta\varphi}{\partial l} \cdot \delta l = \frac{\delta l}{l}. \quad (24)$$

We estimate that the change in the two-way path length due to deformation is less than $\delta l \approx 2$ mm and $l \approx 2$ m, which would result in a relative error of at most 0.1% for the difference phase and, in good approximation, the calculated pressure change.

5. Conclusion

In this work, the two-color, two-arm SDI design is modified to significantly reduce the size and required amount of optical components compared to previous implementations [15,16]. This is primarily achieved by, inter alia, the use of digital two-tone demodulation for an interference signal measured with a single PD. The interferometer can be operated even with little optical power around 11.5 mW and 2.3 mW for the fundamental and SH, respectively.

The system noise and phase stability are investigated experimentally by analyzing the Allan deviation and power spectral density, which determined that the system exhibits both white noise and random drift. The experimental evaluation shows an uncertainty of 3 mrad on the millisecond scale. The long-term drift uncertainty is on the order of 30 mrad. In addition, a worst-case upper bound of uncertainty based on the phasor magnitude obtained during demodulation is derived.

Pressure change measurements were performed over 5 min under laboratory conditions where the calculated data agreed with that of a reference sensor to below 1.5 hPa. For this purpose, the measured phase difference is converted into a relative pressure change via the Ciddor equation. While this shows that the concept can work in general, the achievable accuracy can be further improved before the integration of this device should be feasible for an airborne application.

This includes further investigation and possibly active compensation of the observed drift effects, including an evaluation of the influence of mechanical vibrations on the measured phase due to the two-arm approach. Future measurements with an extended duration on the order of hours might be possible by implementing the demodulation scheme on a field-programmable gate array. This would allow the realistic simulation of the pressure profile of a commercial flight, if the pressure chamber is modified to allow for dynamic venting and pressurization.

Acknowledgments. We thank Anika Moosbrugger for experimental support and Samantha Siegert and Johann Thurn for proof-reading the manuscript.

Disclosures. Oliver Kliebisch, Raoul-Amadeus Lorbeer, Peter Mahnke: German Aerospace Center (P). The authors declare no conflicts of interest.

Data availability. Data underlying the results presented in this paper are not publicly available at this time but may be obtained from the authors upon reasonable request.

References

1. "Standard Atmosphere," ISO 2533:1975.
2. R. Jäckel, G. Gutiérrez-Urueta, and F. Tapia, "A review on Pitot tube icing in aeronautics: Research- design and characterization – future trends," *Flow Measurement and Instrumentation* **81**, 102033 (2021).
3. Y. Cao, W. Tan, and Z. Wu, "Aircraft icing: An ongoing threat to aviation safety," *Aerospace Sci. Technol.* **75**, 353–385 (2018).
4. B. Buchholz, A. Afchine, and V. Ebert, "Rapid, optical measurement of the atmospheric pressure on a fast research aircraft using open-path TDLAS," *Atmospheric Meas. Tech.* **7**, 4775–4813 (2014).
5. R.-A. Lorbeer, O. Kliebisch, P. Mahnke, C. B. Ortega, F. D. Capua, J. Weber, and M. Damm, "Pressure detection via tunable diode laser spectroscopy in the oxygen A-Band," in *Optical Sensors and Sensing Congress* (Optical Society of America, 2020), paper SM1B.6.
6. U. Doll, G. Stockhausen, and C. Willert, "Pressure, temperature, and three-component velocity fields by filtered Rayleigh scattering velocimetry," *Opt. Lett.* **42**, 3773–3776 (2017).
7. B. Edlén, "The Refractive Index of Air," *Metrologia* **2**, 71–80 (1966).
8. J. C. Owens, "Optical Refractive Index of Air: Dependence on Pressure, Temperature and Composition," *Appl. Opt.* **6**, 51–59 (1967).
9. P. E. Ciddor, "Refractive index of air: new equations for the visible and near infrared," *Appl. Opt.* **35**, 1566–1573 (1996).
10. F. A. Hopf, A. Tomita, and G. Al-Jumaily, "Second-harmonic interferometers," *Opt. Lett.* **5**, 386–388 (1980).
11. V. P. Drachev, Y. I. Krasnikov, and P. A. Bagryansky, "Dispersion interferometer for controlled fusion devices," *Rev. Sci. Instrum.* **64**, 1010–1013 (1993).
12. T. Akiyama, M. V. Zeeland, T. Carlstrom, R. Boivin, K. Brunner, J. Knauer, R. Yasuhara, K. Tanaka, H. Liu, Y. Zhou, N. Oyama, A. Sirinelli, K. Urabe, and N. Shirai, "Recent Progress on dispersion interferometers for nuclear fusion and low-temperature plasmas," *Journal of Instrumentation* **15**, C01004 (2020).
13. V. P. Drachev, "Dispersion air interferometer," *Measurement Techniques* **33**, 1125–1127 (1990).
14. F. Brandi and F. Giammanco, "Versatile second-harmonic interferometer with high temporal resolution and high sensitivity based on a continuous-wave Nd:YAG laser," *Opt. Lett.* **32**, 2327–2329 (2007).
15. J. Irby, R. Murray, P. Acedo, and H. Lamela, "A two-color interferometer using a frequency doubled diode pumped laser for electron density measurements," *Rev. Sci. Instrum.* **70**, 699–702 (1999).
16. D.-G. Lee, K. C. Lee, J.-W. Juhn, J.-S. Lee, and Y.-C. Ghim, "The new single crystal dispersion interferometer installed on KSTAR and its first measurement," *Rev. Sci. Instrum.* **92**, 033536 (2021).
17. F. Eddie H. Young and S.-K. Yao, "Design considerations for acousto-optic devices," *Proc. IEEE* **69**, 54–64 (1981).
18. F. Conti, M. Tiberi, F. Giammanco, A. Diaspro, and F. Brandi, "High spatial resolution second-harmonic interferometry," *Laser Phys. Lett.* **10**, 056003 (2013).

19. F. Brandi, F. Wessel, C. M. Lohff, J. R. Duff, and Z. O. Haralson, "Experimental study on the performances of second-harmonic dispersion interferometers at 10.6 μm and 1064 nm for plasma density measurements," *Appl. Opt.* **59**, 8486–8493 (2020).
20. J. Bezanson, A. Edelman, S. Karpinski, and V. B. Shah, "Julia: A fresh approach to numerical computing," *SIAM Rev.* **59**, 65–98 (2017).
21. W. Riley and D. Howe, *Handbook of Frequency Stability Analysis* (National Institute of Standards and Technology, 2008).
22. D. Allan, "Statistics of atomic frequency standards," *Proc. IEEE* **54**, 221–230 (1966).
23. N. El-Sheimy, H. Hou, and X. Niu, "Analysis and Modeling of Inertial Sensors Using Allan Variance," *IEEE Trans. on Instrumentation Meas.* **57**, 140–149 (2008).
24. P. K. Mogensen and A. N. Riseth, "Optim: A mathematical optimization package for Julia," *J. Open Source Softw.* **3**, 615 (2018).